● *Original Contribution*

UNDERSTANDING THE CONTRAST MECHANISM IN ROTATION ELASTOGRAM: A PARAMETRIC STUDY

BASAVARAJAPPA LOKESH,* ANNE M. TEN DAM,[†,‡] CHRIS L. DE KORTE,[†,‡] and ARUN K. THITTAI*

* Biomedical Ultrasound Laboratory, Department of Applied Mechanics, Indian Institute of Technology Madras, Chennai, India;
[†] Medical Ultrasound Imaging Center (MUSIC 766), Radboud University Medical Center, Nijmegen, The Netherlands; and [‡] Physics of Fluids Group, MIRA Institute for Biomedical Technology and Technical Medicine, University of Twente, Enschede, The Netherlands

Abstract—Ultrasound elastography has been found to be useful in different clinical applications. For example, in breast imaging, axial strain elastography provides information related to tissue stiffness, which is used to characterize breast lesions as either benign or malignant. In addition, these lesions also differ in their bonding properties. Benign breast lesions are loosely bonded and malignant breast lesions are firmly bonded to the surrounding tissues. Therefore, only benign breast lesions will rotate/slip on the application of deformation. This rotation of lesions can be visualized with rotation elastography, which utilizes axial and lateral shear strain components. The contrast obtained in rotation elastography depends on various mechanical as well as ultrasound elastography parameters. However, there is no reported work that provides an understanding of the influence of these parameters on the visualized rotation contrast. In this work, the authors studied the rotation contrast by varying the mechanical parameters such as the inclusion *b/a* ratio, relative inclusion-background Young's modulus, amount of applied deformation and orientation of the inclusion. First, the authors performed finite-element analysis to understand the fundamental rotation contrast of the inclusion. Next, rotation elastograms obtained from ultrasound simulations in Field II and experiments on tissue-mimicking phantoms were investigated. Mean contrast was used as a metric to evaluate the quality of rotation elastograms in finite-element analysis, and contrast-to-noise ratio was used in Field II simulations and phantom experiments. The results indicate that rotation contrast was observed only in the case of loosely bonded inclusions. Further, the rotation contrast was found to depend on the inclusion asymmetry and its orientation with respect to the axis of deformation. Interestingly, it was found that a loosely bonded inclusion contrasts with surrounding tissue in rotation elastography, even in the absence of any inclusion-background modulus contrast. (E-mail: akthittai@iitm.ac.in)   © 2018 World Federation for Ultrasound in Medicine & Biology. All rights reserved.

Key Words: Rotation contrast, Ultrasound, Rotation elastography, Bonding, Tissue-mimicking phantom.

INTRODUCTION

Ultrasound (US) elastography (Ophir et al. 1991), a well-established technique, is regularly used in clinical practice to obtain information related to tissue stiffness (Barr 2015; Correas et al. 2013; Shiina 2013). This technique involves the acquisition of US signals from an imaging plane before and after application of a small deformation. This deformation can be applied by a transducer or by an in-body force such as breathing or blood pulse pressure. The signals are analyzed using motion tracking algorithms to estimate the local axial displacements, which are ob-tained along the direction of beam propagation. The gradient of the axial displacements is then used to generate a map of local tissue axial strains, which is referred to as an axial elastogram (Ophir et al. 1999). This technique is widely used and is available in most US scanners because of its high accuracy in estimating tissue displacements in the axial direction. However, in response to the applied deformation, tissue undergoes 3-D motion, which is related to its stiffness and Poisson ratio. Several approaches have been reported that aim to achieve high-precision tracking in both lateral and elevation directions (Awad and Yen 2007; Deprez et al. 2009; Fisher et al. 2010; Konofagou et al. 2000; Treece et al. 2008).

In addition to 3-D motion, benign breast lesions (*i.e.,* loosely bonded lesions) tend to slip at the lesion–background boundary, whereas malignant breast lesions

Address correspondence to: Arun K. Thittai, Biomedical Ultrasound Laboratory, Department of Applied Mechanics, Indian Institute of Technology Madras, Chennai 600036, India. E-mail: akthittai@iitm.ac.in

(*i.e.,* firmly bonded lesions) slip less (Bamber et al. 1988; Chen et al. 1995; Fry 1954; Ueno et al. 1988). Studies have indicated that lesion–background bonding information can be visualized using shear strain elastography (Konofagou et al. 2000) or axial-shear strain elastography (Thitaikumar et al. 2007, 2008; Thittai et al. 2011). The total shear strain is the sum of axial- and lateral-shear strain components, which are computed by taking the gradient of axial (lateral) displacements in the lateral (axial) direction, respectively.

The above-mentioned works characterized shear strain only at the inclusion boundary by assuming a circular geometry, which may be considered a reasonable first-order simplification. However, an interesting behavior observed and reported in the applied materials literature prompted further investigation to exploit the combination of different boundary conditions and asymmetric inclusion geometry. Specifically, the behavior of the elastic stress and strain fields in and around an elliptical inclusion were found to be interesting, as discussed below.

Eshelby (1957, 1961) derived an analytical solution to the elasticity problem of a stiff elliptical inclusion embedded in a softer background, assuming perfectly firm bonding conditions. Later, Mura and Furuhashi (1984) reported on the behavior of the elastic fields of ellipsoidal inclusions with slip (loosely bonded) conditions at the inclusion–background boundary. Their results indicated that there is rigid rotation between the matrix and the inclusion and that the solution is valid only if the corresponding axes of the ellipsoidal inclusion are not equal. Later, Lubarda and Markenscoff (1998) tried to explain this situation, which they called "unusual," in nearly circular/ spheroidal inclusions under shear eigenstrain and provided elegant mathematical and physical explanations. They reported that the presence or absence of shear strain inside an elliptical inclusion depends on the combined effect of the applied shear eigenstrain, the inclusion aspect ratio and its orientation.

The slip/rigid rotation of the inclusion can be captured in US measurements by utilizing the estimates of shear strains and the equation (Timoshenko and Goodier 1970)

$$W_{x,y}(\text{rotation}) = 0.5\left(\frac{\partial v}{\partial x} - \frac{\partial u}{\partial y}\right) \qquad (1)$$

where u is the lateral displacement, v is the axial displacement and x and y are the lateral and axial directions, respectively.

To image the rotation, accurate displacement estimates in both the axial and lateral directions are required. Because of the inherent limitations in estimating lateral displacements with the same precision as for axial displacements, Thittai et al. (2010) proposed using only the first term of eqn (1) (*i.e.,* the axial-shear strain compo-

nent). They reported that non-zero axial-shear strain occurs inside the lesion when a loosely bonded asymmetric lesion is oriented non-normally to the axis of deformation, which was referred to as *fill-in* (Galaz et al. 2009; Thittai et al. 2010). Thus, the *fill-in* captured in the axial-shear strain elastogram (ASSE) was used as a first-order approximation of rotation undergone by the inclusion. Although the *fill-in* observed in ASSEs has been found to be of superior quality and observable in freehand *in vivo* breast lesions (Chintada et al. 2017), it does not have a simple physical interpretation. The physical interpretation of *fill-in* as capturing the angular deformation of a loosely bonded inclusion, along the vertical direction, may not be as intuitive compared with interpreting the physical rotation undergone by the inclusion because of slip. Hence, the imaging of inclusion rotation directly may be more attractive and easy to interpret than an ASSE (Thittai et al. 2012). Toward this end, the authors' group recently imaged inclusion rotation with improved image quality by employing synthetic transmit aperture and spatial compounding techniques (Kothawala et al. 2017; Lokesh et al. 2017). Several groups have reported different methods to improve the precision of lateral displacement tracking for elastography (Hansen et al. 2010; Konofagou and Ophir 1998; Techavipoo et al. 2004), which may also lead to reliable estimation of the rotation.

To the best of the authors' knowledge, however, no study in the literature has investigated and reported the parameters that affect contrast in the rotation elastogram (RE). An understanding of the fundamental contrast mechanism involved in REs may be of interest with respect not only to ultrasound elastography, but also to other modalities that may exploit this aspect. In this work, the authors report on the effect of mechanical parameters that affect the contrast of the RE through finite-element method (FEM) simulation, ultrasound elastography simulation and *in vitro* experiments performed on tissue-mimicking phantoms. The parameters investigated in this study are asymmetry or aspect ratio of the lesion (*b/a* ratio), inclusion orientation with respect to the axis of deformation, relative Young's modulus of the lesion–background boundary and applied deformation.

METHODS

Finite-element method model

A 2-D plane strain model was used to build a phantom in COMSOL Multiphysics (COMSOL AB, Stockholm, Sweden) with the overall dimensions 50 (height) × 50 (width) mm. The phantom geometry consisted of a single cylindrical inclusion with elliptical cross section at the center of the phantom. A constant Poisson ratio of 0.495 and density of 1060 kg/m^3 were set for the inclusion and the background materials. By default, COMSOL software makes a union between the inclusion and background,

which models a firmly bonded inclusion. However, COMSOL allows users to define contact elements and assign a static coefficient of friction (COF) at the inclusion–background boundary to simulate different types of bonding inclusions (Thitaikumar et al. 2007). The phantom was subjected to uniaxial compression by loading it from the top. A point located at the bottom on the axis of lateral symmetry of the model was constrained in the axial and lateral directions to avoid any rigid motion of the whole model. The lateral edges of the phantom were kept free to allow motion in the lateral direction.

The parameters that affect the contrast in REs considered in this study are as follows:

1. Relative (inclusion to background) Young's modulus contrast, which was varied from 1 to 3 in the steps of 1
2. Aspect ratio (b/a), the values of which used in this study were 0.63 (7.2 mm/11.4 mm), 0.74 (8.1 mm/10.9 mm), 0.86 (9.0 mm/10.5 mm) and 1(10 mm/10 mm)
3. Orientation of inclusion with respect to the axis of compression (*i.e.,* 45°, 30°, 15°, 10°, 0°).
4. Level of uniaxial deformation, which was varied from 1% to 5% in the steps of 1%.

Each parameter was investigated separately by varying the COF from 0.01 to 100, having 41 non-uniformly spaced values and setting the other parameters to default values (b/a ratio = 0.74, angle = 45°, relative Young's modulus = 2, and deformation = 2%). Note that the b/a values chosen here were based on the approximate dimensions of the manufactured inclusions that were used in experiments described later in this section.

Field II simulation

Ultrasound simulations were carried out using Field II software (Jensen 1996). A linear array transducer was simulated with values of different parameters as listed in Table 1. The spatial impulse response was defined for the simulated transducer, and transducer elements were excited using 2 cycles of sinusoid during transmission. The computer phantom as specified in the previous paragraph was taken, with a distance "z_start" of 1 mm between the transducer and phantom surface to avoid calculation error in

Table 1. Transducer parameter values used in the Field II simulations

Transducer parameter	Value
No. of elements	192
Active elements per transmit/receive	64
Pitch	0.3 mm
Element width	0.275 mm
Element height	4 mm
Center frequency	5 MHz
Sampling frequency	40 MHz

Field II. The phantom was filled with randomly distributed scatterers with Gaussian distributed amplitude. Scatterer density was maintained at 10 scatterers per wavelength to generate an ultrasound image with fully developed speckle. The computer-generated phantom was imaged using a linear array transducer with the conventional focused beamforming technique. In this technique, the active aperture was excited in such a way that beams were focused at a depth of 25 mm, and reflected echoes from scatterers were received by the same active aperture and then beamformed using dynamic receive focusing with depth-dependent apodization to obtain a single A-line (*i.e.,* received voltage trace). This A-line was generated by convolving the pulse-echo response (*i.e.,* two-way response) of the transducer with the medium consisting of randomly distributed scatterers (Jensen 1991). Next, the active aperture was moved by one transducer element at a time, 128 times, to acquire the 128 A-lines. These A-lines were arranged next to each other in the lateral direction to obtain pre-compression radiofrequency (RF) data. Thereafter, a phantom with displaced scatterers was generated by adding the displacement maps from the FEM simulation to the scatterers of the existing computer phantom. The displaced scatterers were imaged to obtain the post-compression RF data. To reduce the computation time, US simulations were performed only for eight values of the COF: 0.01, 0.05, 0.1, 0.18, 0.2, 0.3, 1 and 100.

Tissue-mimicking phantom

All tissue-mimicking phantoms were made using the agar–gelatin–water mixture recipe previously described in the literature (Hall et al. 1997; Kallel et al. 2001). These phantoms were prepared using the cuboid mold of overall dimensions $50 \times 50 \times 60$ mm (height × width × length) with a single elliptical cylinder inclusion (60 mm in length) running along the length through the cuboid. The phantom material was prepared by mixing gelatin and agar in weight percentage with de-ionized water at 80 °C. To investigate the contrast in the RE, two kinds of phantoms were prepared (*i.e.,* firmly and loosely bonded inclusion phantoms). To obtain a firmly bonded inclusion phantom, first the background was manufactured, and after 12 h, inclusion material was poured into the cylindrical hole left in the background phantom after removal of the insert. To obtain a loosely bonded inclusion, inclusion and background were manufactured separately, and then the inclusion was inserted into the background, which had an elliptical cylinder hole. Phantoms were manufactured by changing the Young's modulus contrast, b/a ratio and orientation of the inclusion for both firmly and loosely bonded inclusion phantoms. Backgrounds of all the phantoms were manufactured using 5% by weight gelatin and 3% by weight agar. To study rotation contrast as a function of Young's modulus, we varied the Young's modulus of the

Table 2. Relative gelatin and agar concentrations used to manufacture phantoms with different YMC values

	Agar (% by weight)	Gelatin (% by weight)
YMC1		
Background	3	5
Inclusion	3	5
YMC2		
Background	3	5
Inclusion	3	10
YMC3		
Background	3	5
Inclusion	3	15

YMC = Young's modulus contrast.

inclusion with respect to the background by changing the percentage weight of gelatin (Kallel et al. 2001). Gelatin and agar concentrations used to manufacture three different phantoms with varying Young's modulus contrast (YMC) values are listed in Table 2. To study rotation contrast as a function of *b/a* ratio, the authors prepared phantoms by varying the shape of the inclusion by changing the ratio of minor to major axis radii of the inclusion inserts. To study rotation contrast as a function of inclusion orientation with respect to the axis of deformation, different phantoms were prepared with inclusions oriented at 45°, 30°, 15° and 0°.

Data acquisition

Experiments were performed on the phantoms using the SONIX TOUCH Q + (Ultrasonix, Analogic Corporation, Peabody, MA, USA) scanner with a linear array transducer (L 14-5/38). The operating frequency and sampling frequency of the scanner are 5 and 40 MHz, respectively. The RF data were collected using conventional focused linear array technique. Pre-compression RF data were obtained after placing a small load on top of the phantom to avoid any floating motion of the phantom, which was submerged in water during the experiment. Note that this small pre-loading was not modeled in simulations. Thereafter, post-compression RF data were obtained by subjecting the phantom to 2% compression. The entire phantom was subjected to controlled compression using a 12 × 12-cm plate. The aforementioned experiments were repeated for different planes, which were separated by a distance of 0.5 mm along the elevational direction, to obtain five different realizations of the RE. Note that the data were acquired within 24 h of the manufacture of phantoms, to reduce the effect of phantom degradation.

Displacement tracking

The local axial and lateral displacements were obtained by applying a 2-D multilevel block-matching algorithm (Lindop et al. 2007; Lopata et al. 2009a; Shi and Varghese 2007; Thittai et al. 2010). Specifically, in our implementation (Thittai et al. 2010), the algorithm selects a reference block in the pre-compressed RF data and searches for its optimal match in the post-compressed RF data using normalized cross-correlation. To improve computation time and sensitivity, the algorithm was divided into three levels: two coarse levels and one fine level. The first coarse-level displacements were taken as the initial point to search the second coarse-level displacements, which were subsequently used to estimate the finer-level displacements. Before the block-matching step, pre- and post-compression RF data were interpolated by a factor of 2 in the lateral direction. The coarse levels use the envelope of the RF data to estimate displacements. The envelope data were decimated by factors of 4 and 2 in the axial direction in the first and second coarse levels, respectively. In contrast to the coarse levels, the finer level used RF data without decimation. Cosine and parabolic interpolations were used in the axial and lateral directions, respectively, to obtain subsample displacement estimation. The axial block size used in the first coarse, second coarse and fine levels were 25λ, 5λ and 3λ, respectively. The lateral block size of 0.6 mm, which corresponds to 4 A-lines, was used at all levels (after interpolation). In the first and second coarse levels, there was no overlap of blocks. However, in the finer level, the overlap was 60% and 75% of the block size used in the axial and lateral directions, respectively. The extents of axial search used in the first coarse, second coarse and fine levels were 25%, 50% and 50% of the block sizes used, respectively. The extent of lateral search was 50% of the block size used at all levels. Finally, the RE was obtained from the finer-level displacements using eqn (1).

Rotation contrast estimation

In the case of the FEM, only the rotation contrast between the inclusion and the background was estimated as a metric, and not contrast-to-noise ratio (CNR), because FEM simulation does not involve any measurement noise, unlike ultrasound simulations and experiments. The mean rotation value from a region of interest (ROI) inside the inclusion was calculated from the FEM-predicted rotation image. This mean value represents the amount of rotation undergone by the inclusion. The ROI considered was a 4 × 4-mm square block, which was kept at the center of the inclusion.

Contrast-to-noise ratio estimation

To quantify image quality, the CNR was calculated from the REs obtained in Field II simulations and *in vitro* experiments using the equation:

$$CNR = \frac{2\left(\mu_{inclusion} - \mu_{background}\right)^2}{\left(\sigma_{inclusion}^2 + \sigma_{background}^2\right)} \qquad (2)$$

where $\mu_{inclusion}$ and $\mu_{background}$ are the mean values of the rotation estimates obtained from an ROI inside and outside the inclusion, respectively, and σ is the corresponding standard deviation for both regions. The ROIs used were two 4×4-mm square blocks inside the inclusion and the background at the same depth.

RESULTS

Simulation

Figure 1 illustrates the axial displacements, lateral displacements and rotation elastograms for the firmly bonded inclusion case, obtained from FEM and Field II simulations. Note the absence of contrast in the RE because there is no slip in the lesion–background boundary.

Figure 2 illustrates the axial displacements, lateral displacements and rotation elastograms for the loosely bonded inclusion case, obtained from FEM and Field II simulations. It can be observed that unlike the firmly bonded inclusion case in Figure 1, the rotation contrast appears conspicuously in the case of the loosely bonded inclusion.

In Figure 3 are 3-D plots of contrast values calculated from rotation images obtained in FEM for different COFs. For all the different parameter settings, contrast values are high for a low COF, start decreasing as the COF increases and become zero for COF values >1. This suggests that COFs >1 essentially model a firmly bonded inclusion case in FEM software. Figure 3(a) illustrates the change in contrast values of rotation images when the inclusion orientation is changed with respect to the axis of deformation. It can be observed that there is no rotation contrast when the minor axis of the inclusion is aligned with the direction of applied deformation (*i.e.,* 0°). This holds for all COFs. However, even for a small inclusion rotation angle, the rotation contrast is present, and these contrast values increases as the inclusion orientation increases from 0° to 45°. Figure 3(b) illustrates the presence of rotation contrast even when there is no Young's modulus contrast between inclusion and background. In fact, the rotation contrast values vary only slightly for the different relative Young's moduli. Figure 3(c) illustrates the change in rotation contrast values when the phantom is subjected to different levels of deformation. It can be observed that rotation contrast values start to increase as the percentage of deformation increases for any given COF value <1. Also, rotation contrast values decrease to nearly zero as the COF increases beyond 1 for any given deformation level. Finally, the effects of variation of the aspect
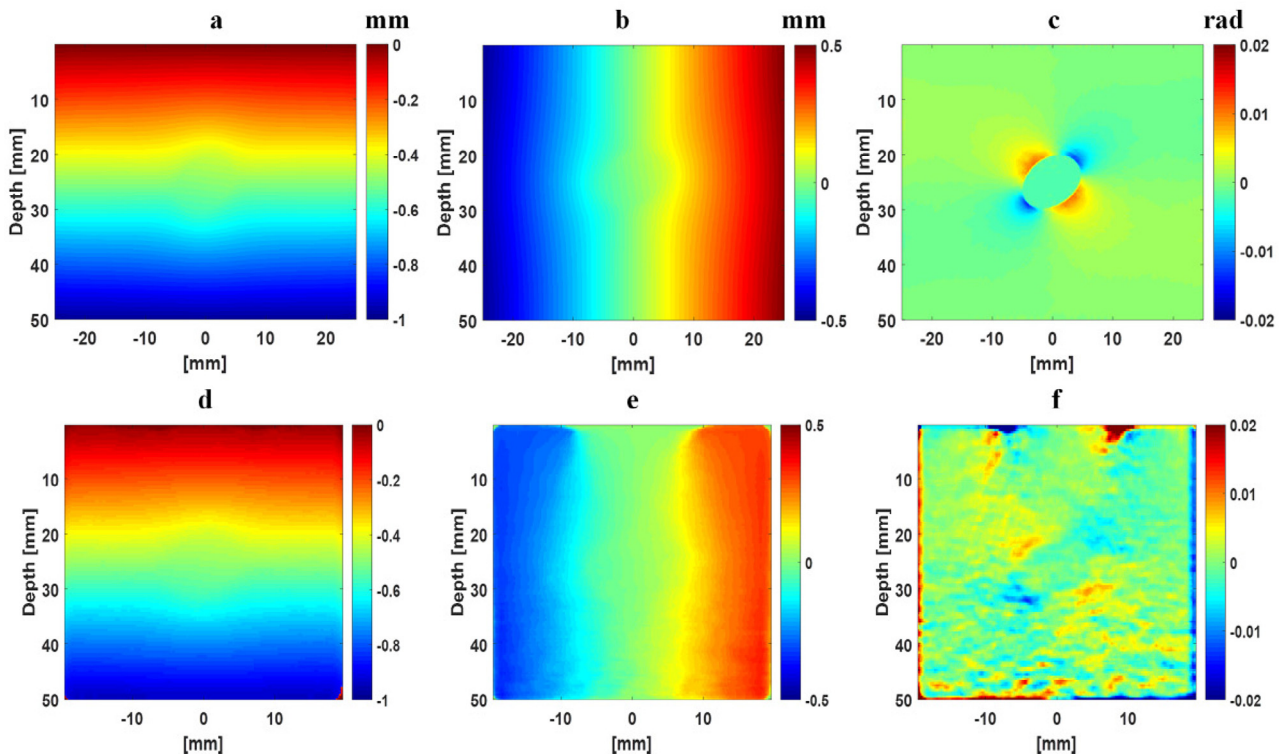

Fig. 1. Simulation: Axial displacements (first column), lateral displacements (second column) and rotation elastograms (third column) of a firmly bonded inclusion obtained from finite-element modeling (a–c) and Field II (d–f). Note that the images were obtained using the default values of the parameters (*i.e.,* relative Young's modulus = 2, *b/a* ratio = 0.74, angle = 45°, axial deformation = 2%). The Field II images are averages of five different planes.
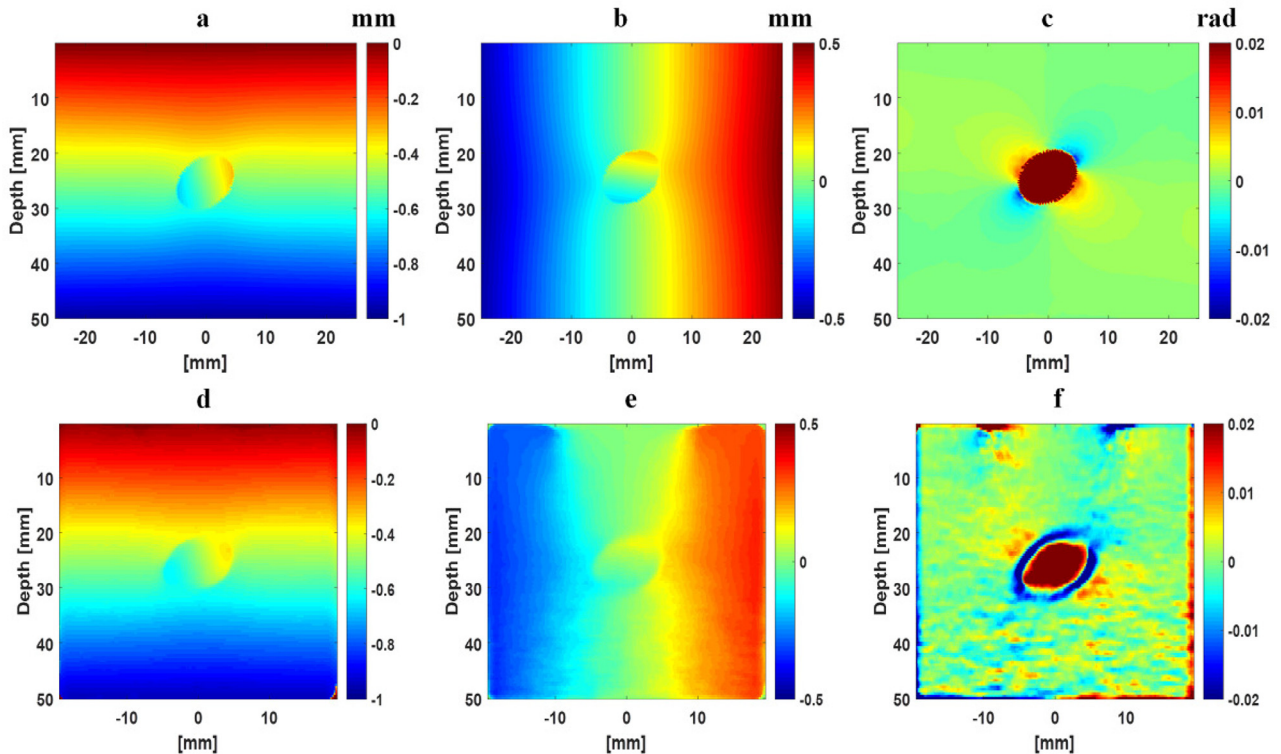
Fig. 2. Simulation: Axial displacements (first column), lateral displacements (second column) and rotation elastograms (third column) of a loosely bonded inclusion obtained from finite-element modeling (a–c) and Field II (d–f). Note that the images were obtained using the default values of the parameters and a coefficient of friction of 0.18. The Field II images are averages of five different planes.

ratio (*b/a*) on the contrast of rotation images are illustrated in Figure 3(d). A non-zero rotation contrast can be seen at all aspect ratios of the inclusions, except for a ratio of 1. It can be seen that rotation contrast is very sensitive to the change in inclusion shape from circular to elliptical. In addition, the authors can see more rotation contrast in nearly symmetric inclusions (*i.e., b/a* = 0.86) than in more asymmetric inclusions for low COFs. The contrast drops with an increase in COF for any given *b/a* ratio.

The ideal fundamental rotation undergone by the inclusion for different parameters was captured using the rotation contrast metric and is depicted in Figure 3. The contrast that can be obtained in the RE obtained with US simulations is illustrated in Figure 4, where CNR is used as a metric. This CNR is a combination of the ideal contrast values that were quantified with the FEM simulations and the noise in the estimation process using the US signal. Figure 4(a) illustrates the change in CNR values for different inclusion orientations. The CNR value is close to 0 (no rotation) when the inclusion orientation is 0°, as the authors observed in FEM simulations. Further, for COFs <0.1 the CNR values are high in the case of small inclusion orientations (*i.e.,*10° and 15°), whereas they are low in the case of other inclusion orientations (*i.e.,* 30° and

45°). This is probably due to the limitations in the displacement tracking algorithm, which fails to capture the large rotations undergone by the inclusions. Figure 4(b) illustrates the CNR values for different relative Young's moduli. An interesting observation is the presence of rotation contrast even in the absence of relative modulus contrast for a loosely bonded inclusion, as already found in the FEM simulations. Figure 4(c) illustrates the change in CNR values as a function of percentage deformation, which follows a trend similar to that of FEM simulations until 2% deformation. For higher deformation values, the CNR decreases. The decrease in CNR for increasing strain values is probably due to signal decorrelation effect, which is described and well documented as the strain filter concept in US elastography (Varghese and Ophir 1997). Given that the strain filter concept has been well reported in the literature, the authors did not illustrate or quantify the normalized cross-correlation coefficients. Nevertheless, the ROI was chosen such that it avoids the decorrelated pixels at the inclusion boundary. Figure 4(d) illustrates the change in CNR values for different *b/a* ratios. As noted in results from the FEM, Field II simulations also indicate that there is no rotation for a *b/a* ratio of 1 and there is more rotation in the case of nearly symmetric inclusions. It can be
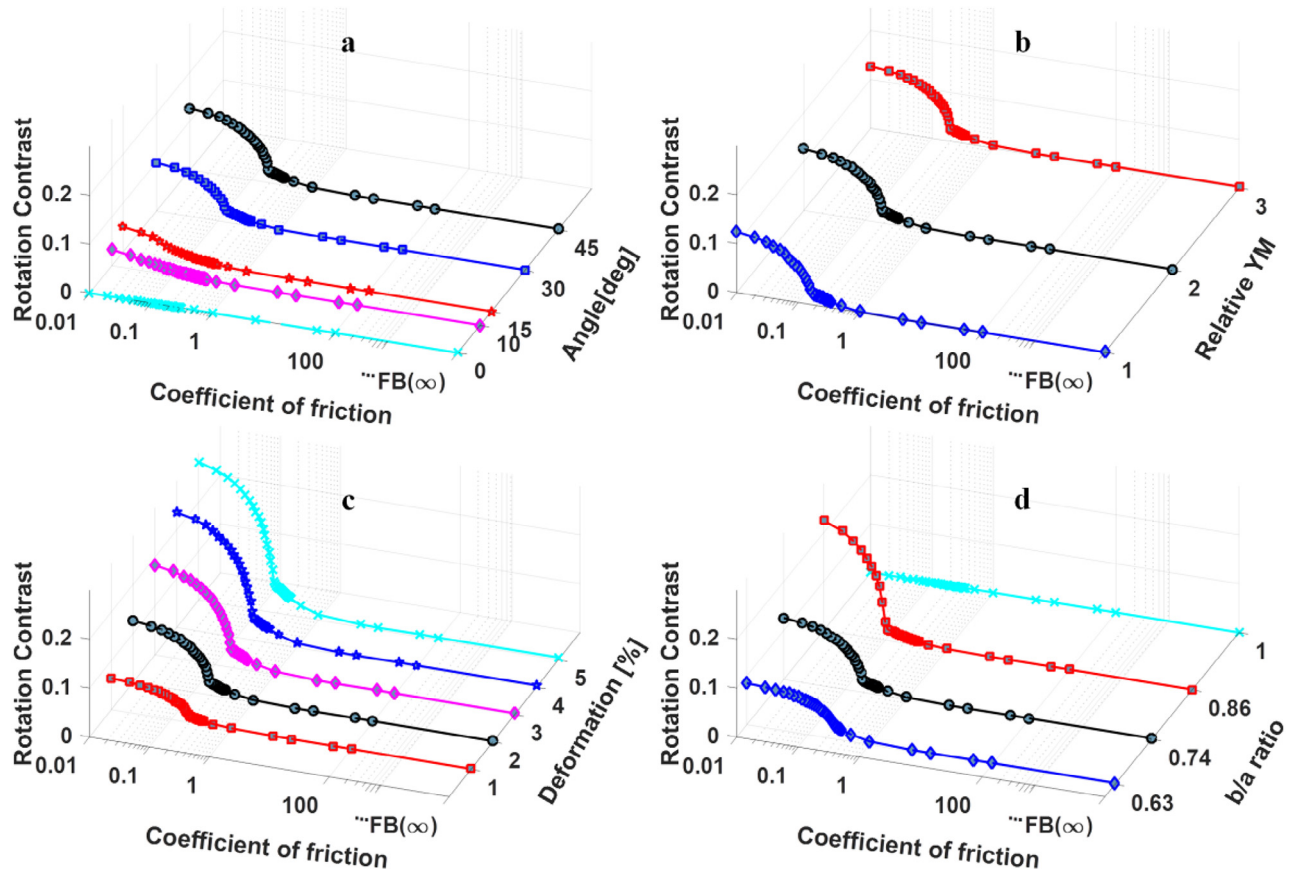
Fig. 3. Plots of contrast values computed from the rotation images obtained from the finite-element modeling simulations for different parameters: (a) relative orientation of inclusion, (b) relative YM, (c) percentage deformation, (d) *b/a* ratio. FB = firmly bonded inclusion; YM = Young's modulus.

noted that for all the different parameters, the CNR values are low for COFs of 0.01 and 0.05 and thereafter follow a trend similar to that observed in the FEM results, except for the inclusion orientation and deformation. This highlights the need to develop robust displacement tracking algorithms that can work well in the presence of displacement discontinuity caused by slip boundary.

Experiment

Figure 5 illustrates the axial displacements, lateral displacements and rotation elastograms for the firmly bonded inclusion obtained from experiments performed on a tissue-mimicking phantom. We can observe similar behavior in the RE obtained from the experiment, that is, the absence of any rotation contrast, as noted in the RE from the FEM as well as the Field II simulations.

Figure 6 illustrates the axial displacements, lateral displacements and rotation elastograms for the loosely bonded inclusion obtained from experiments performed on a tissue-mimicking phantom. We can observe the presence of contrast in the RE obtained from the experiment similar

to that observed in the REs from the FEM and Field II simulations.

In Figure 7 are plots of CNR values computed from experimentally obtained REs for different parameter settings. Figure 7(a) illustrates a low CNR value (*i.e.,* nearly zero) for 0° inclusion orientation that increases as the inclusion orientation increases with respect to the axis of deformation. The experimental results also indicate that the CNR values obtained from the RE are practically independent of relative Young's modulus contrast (Fig. 7b). Figure 7(c) illustrates the CNR values obtained from rotation elastograms for phantoms subjected to different levels of deformation. It depicts a low CNR value for 1% deformation, caused by the minimal rotation of the inclusion. The CNR values start to increase as the deformation increases and then start to decrease for deformation values >2%. For these strain values, the decorrelation noise starts to dominate, as was also noted in relation to Figure 4(c). Figure 7(d) illustrates that the CNR values remain almost similar for the *b/a* ratios 0.63 and 0.74 and decrease as the *b/a* ratio approaches 1.
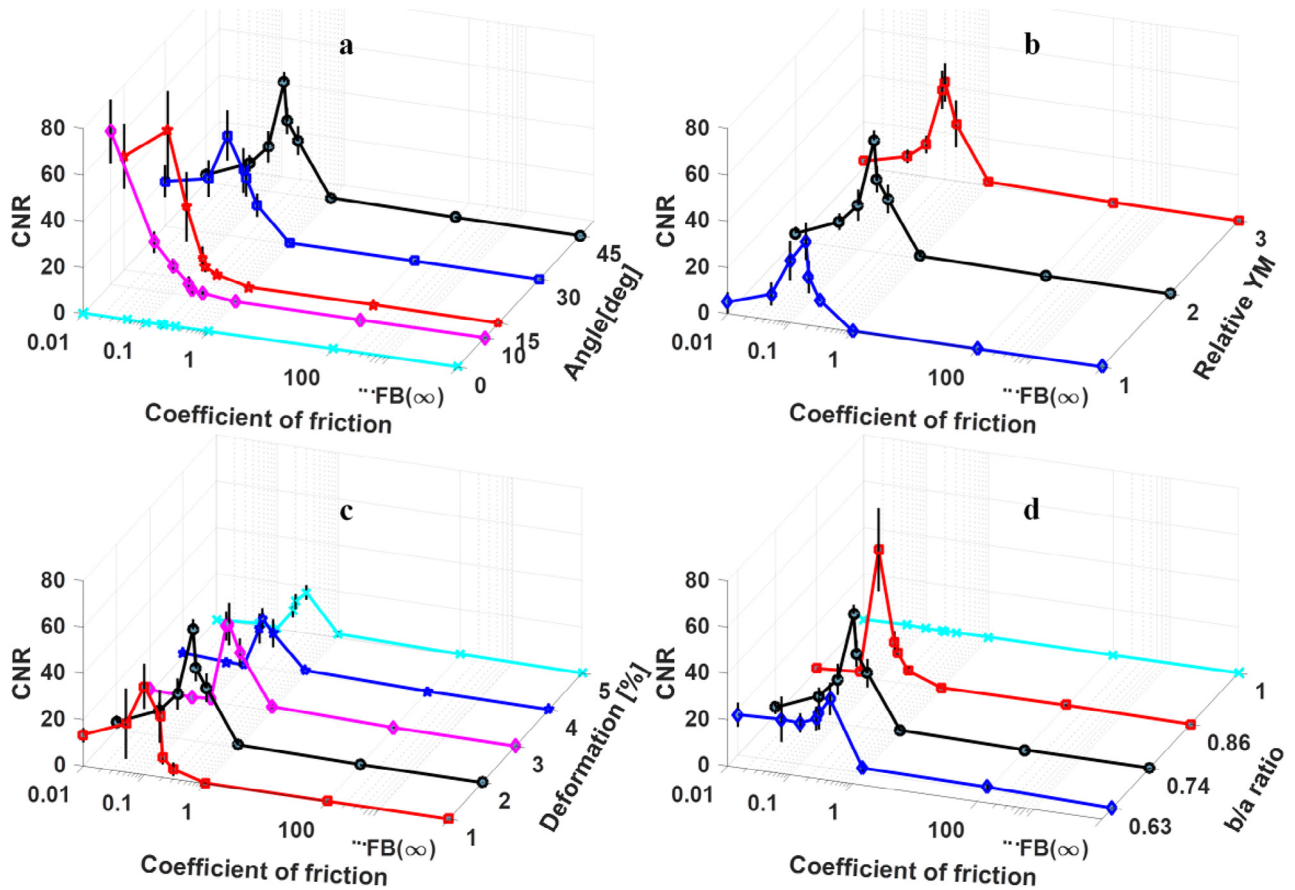
Fig. 4. Plots of CNR values computed from the rotation elastograms obtained from the Field II simulations for different parameters: (a) relative inclusion orientations, (b) relative YM, (c) percentage deformation, (d) *b/a* ratio. The means and standard deviations were calculated from five independent realizations of the rotation elastogram. CNR = contrast-to-noise ratio; FB = firmly bonded inclusion; YM = Young's modulus.
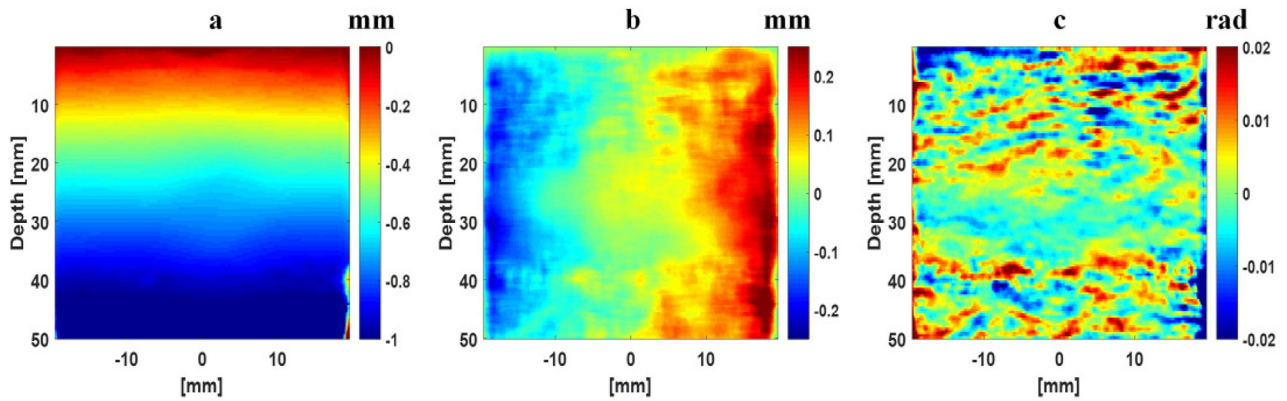

Fig. 5. Experiment: Axial displacements, lateral displacements and rotation elastograms of a firmly bonded inclusion obtained from the experiments performed on a tissue-mimicking phantom. Note that the images were obtained using the default values for the different parameters (*i.e.,* Young's modulus contrast 2, *b/a* ratio = 0.74, angle = 45°, axial deformation = 2%) and are averages over five different planes.
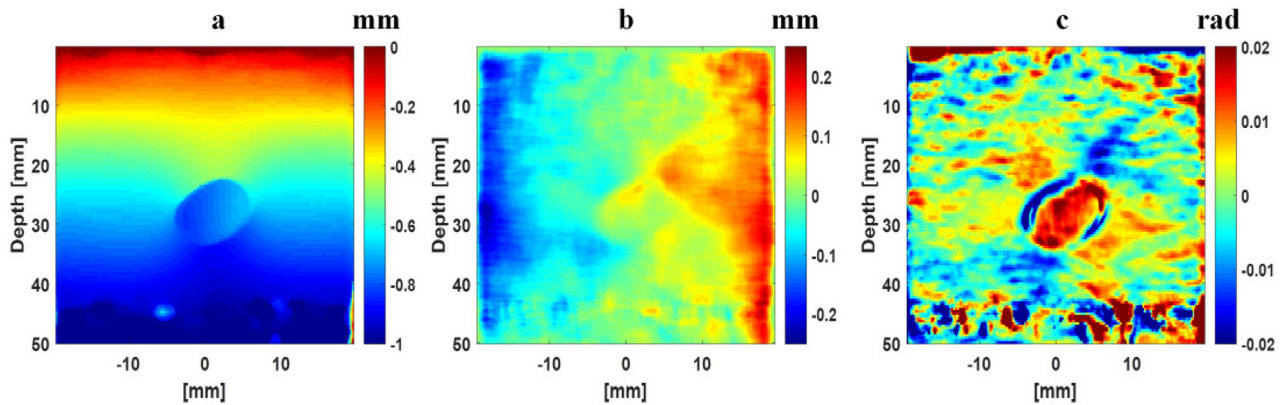
Fig. 6. Experiment: Axial displacements, lateral displacements and rotation elastograms of a loosely bonded inclusion obtained from the experiments performed on a tissue-mimicking phantom. Note that the images were obtained using the default values of the parameters and are averages over five different planes.
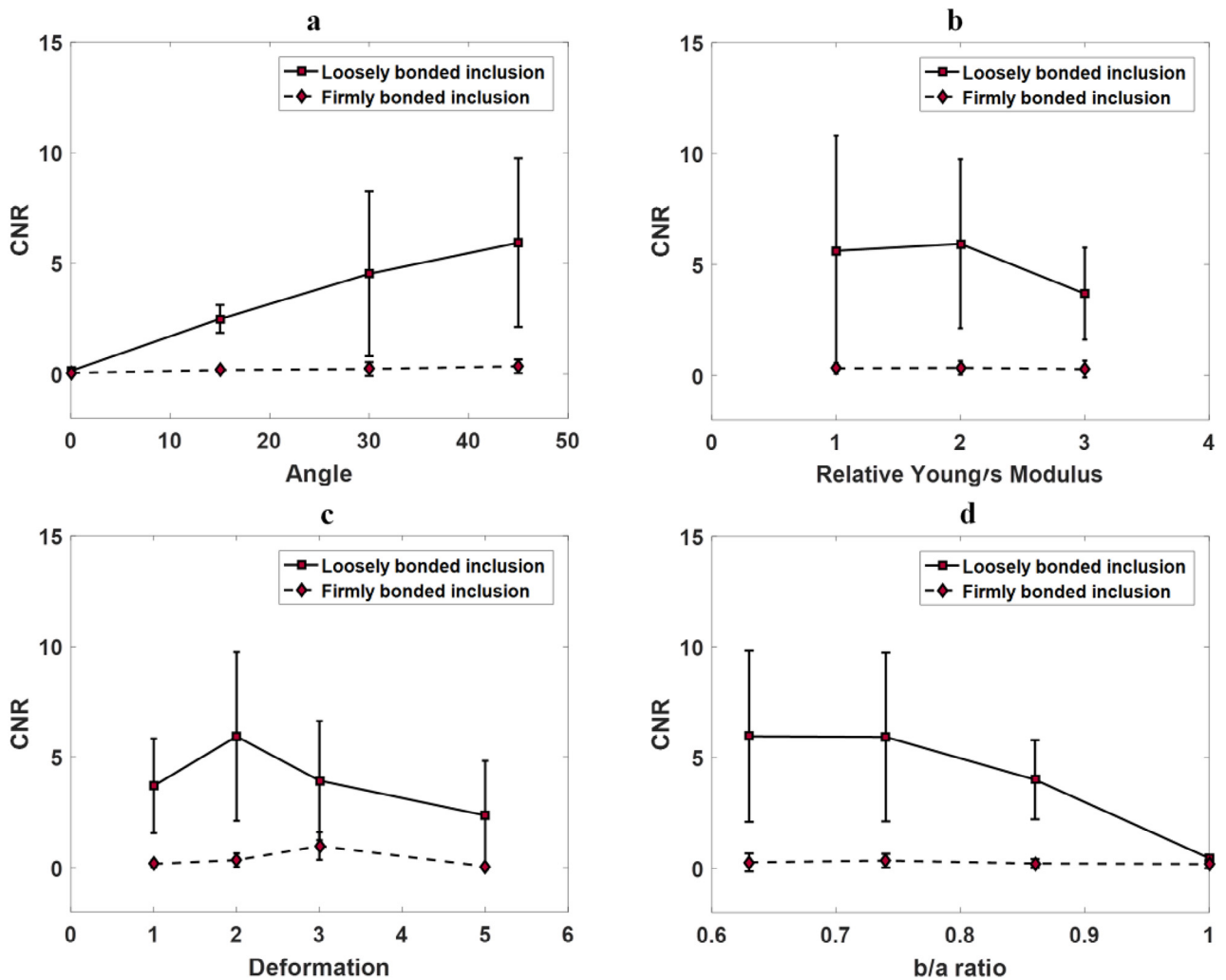

Fig. 7. Plots showing the CNR values obtained from the experiments performed on the tissue-mimicking phantoms for different mechanical parameters: (a) relative Young's modulus contrast, (b) inclusion's relative orientation, (c) percentage deformation, (d) *b/a* ratio. The means and standard deviations were calculated from five different realizations of the rotation elastogram. CNR = contrast-to-noise ratio.

DISCUSSION

In this study, we performed parametric analysis to understand the fundamental contrast mechanism in US rotational elastography using FEM simulations, Field II simulations and phantom experiments of both loosely and firmly bonded inclusion cases. The main focus of our study was to investigate and understand what parameters generate a true contrast (obtained using FEM) and how much of it can be captured using ultrasound imaging system. Specifically, we varied only the mechanical parameters like deformation, aspect ratio, inclusion orientation and relative Young's modulus and did not focus on the ultrasound or signal processing parameters, which are left for future work. The rotation contrast is observed only in the case of loosely bonded inclusions because of the slipping/rotation of the inclusion, whereas, there is no such contrast in the case of firmly bonded inclusions. Most interestingly, the results further indicate that rotation contrast is practically independent of the inclusion–background modulus for the ranges considered. Nevertheless, rotation contrast depends on the bonding conditions, orientation, aspect ratio and applied deformation. In particular, rotation contrast was seen when the inclusion was slightly asymmetric, non-normally oriented and loosely bonded to the background. The rotation contrast starts to appear even for orientation angles as small as 10°. It must be noted that in reality, we do not have control over any of the mechanical parameters studied here, except for applied deformation. Nevertheless, our understanding obtained in this study can be used to our advantage in some applications like breast imaging. For example, it is known that most benign breast lesions tend to be ellipsoidal in shape (Stavros et al. 1995) and are loosely bonded to the surrounding tissue. Because most of the lesions are located in the ducts that are directed from the inner breast tissue to the nipple, most lesions have an orientation that differs from the deformation direction. Furthermore, different inclusion orientations with respect to the axis of deformation can be achieved by tilting the probe. Therefore, with subtle adjustments, we can generate contrast in the RE to visualize even the barely stiff lesions, which are challenging to visualize in standard elastograms, in strain imaging as well as in shear wave elastography.

One major discrepancy between ideal FEM predictions and Field II US simulation results was the low CNR values obtained in the latter case for COFs <0.1. This discrepancy may be due to the limitations of the displacement tracking algorithm; that is, when you have a large rotation (at low COF) for a given percentage deformation, *b/a* ratio and orientation, the resulting 2-D displacement cannot be tracked accurately because of the large discontinuity in the displacement in the lateral direction. These problems might be partly solved as previously discussed by Lopata et al. (2009a, 2009b), who reported that coarse-to-fine displacement estimation with aligning and stretching (re-correction) provides accurate displacements for larger deformations. In their follow-up work, they reported further improvement in the displacements using the deformed kernel shape, especially when shearing and rotation movements were present (Lopata et al. 2009b). However, these methods do not address the issue of large discontinuities in the displacement in the axial direction, and new methods are required to eliminate this problem. On the other hand, it must be stated that COF values <0.1 are seldom present *in vivo* when the application is lesion detection. Nevertheless, it is clear that there is enough merit in working to improve the quality of RE. In addition to working on displacement tracking algorithms, the use of different imaging techniques, like synthetic aperture-based imaging or spatial compounding, can be explored (Hansen et al. 2010; Kothawala et al. 2017; Lokesh et al. 2017).

In simulations, we also observe that there is more rotation contrast in nearly symmetric inclusions (*i.e.*, *b/a* = 0.86) at low COFs, whereas more asymmetric inclusions exhibit considerable rotation contrast even for COF
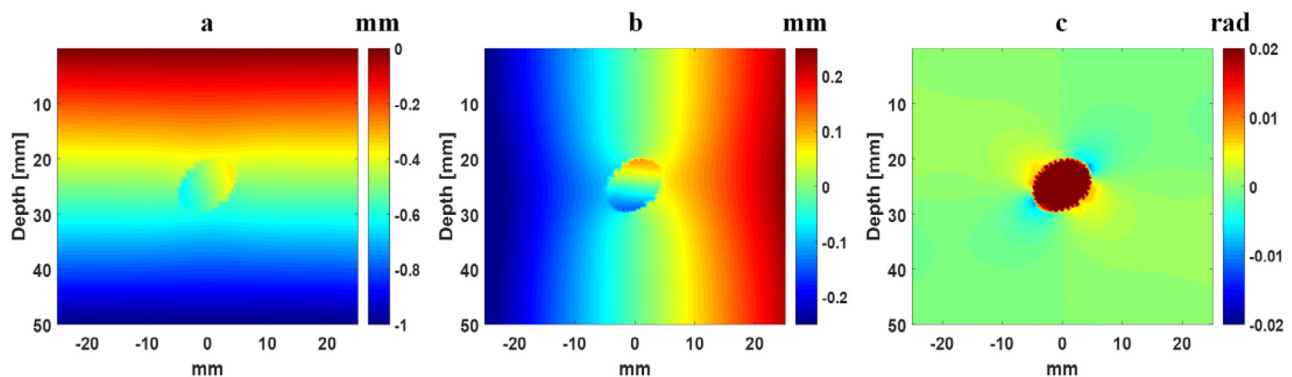

Fig. 8. Simulation: (a) Axial displacements, (b) lateral displacements and (c) and rotation elastogram of a loosely bonded inclusion obtained from a center slice of the 3-D finite-element model. Note that the images were obtained using the default values of the parameters and a coefficient of friction of 0.18.
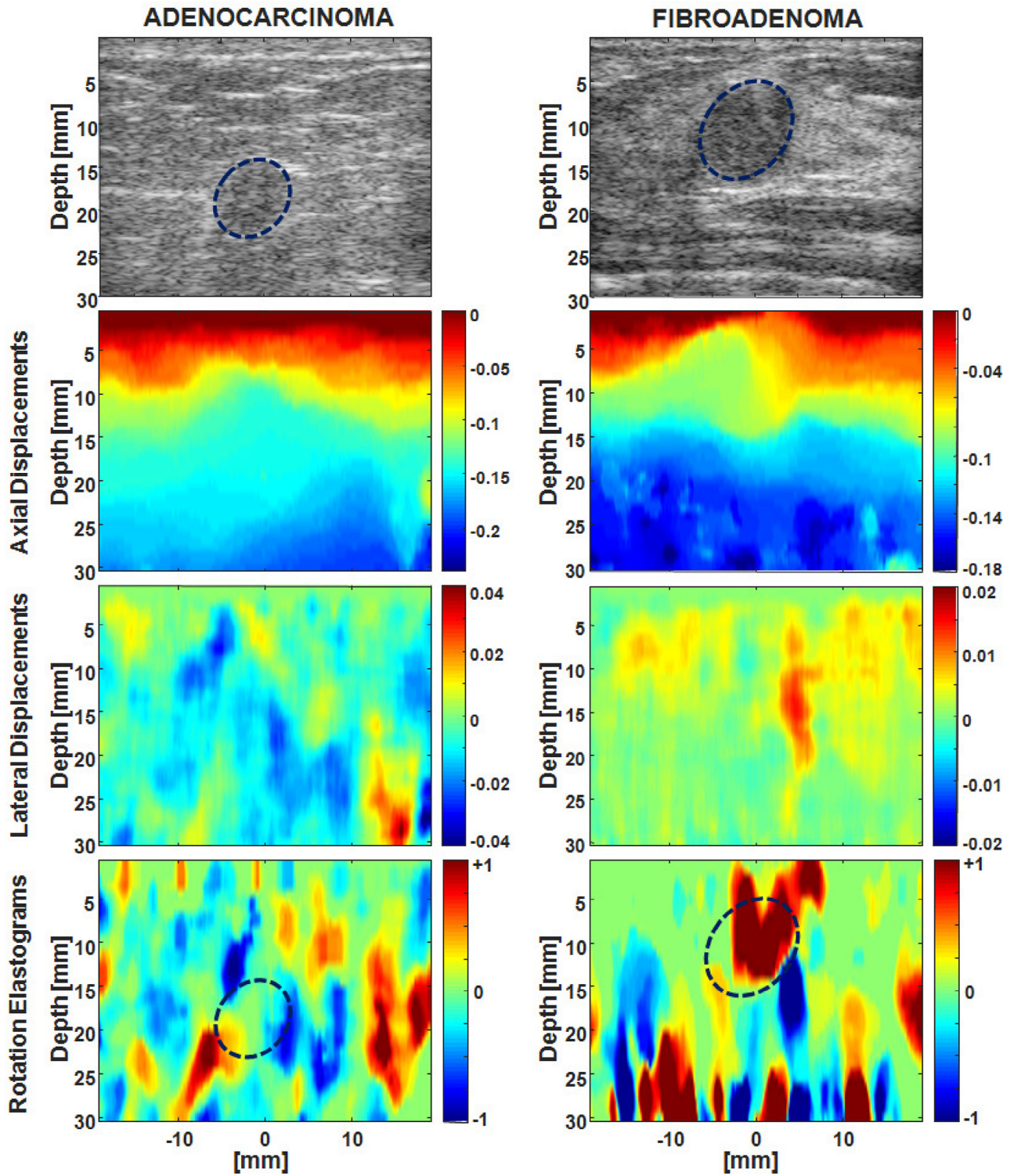
Fig. 9. Example *in vivo* data for the sonogram, axial displacement image, lateral displacement image and rotation elastogram of an invasive adenocarcinoma (first column) and a benign fibroadenoma (second column). The displacement images and rotation elastograms are averages of eight frames.

values >2. However, the low CNR values observed in the experiments for nearly symmetric inclusion are similar to those in the simulations for COFs ranging from 0.18 to 0.3. Thus, based on the observations from the results it can be stated that the COF of the loosely bonded inclusion phantom used in the experiments could be in the range 0.18 to 0.3. Note that the exact COF of the loosely bonded inclusion phantom is not known, and the process to make one is still an open challenge.

In this study, we used a 2-D phantom with plane strain approximation in simulations; however, phantoms containing cylindrical inclusions in experiments and *in vivo* (*e.g.,* breast lesions) are 3-D and may have some out-of-plane rotation depending on the orientation of the inclusion with respect to the axis of deformation and plane of imaging. Figure 8 illustrates the results obtained from a center slice of a 3-D FEM model, which are similar to the results obtained from the 2-D plane strain model (Fig. 2a–c), except a change in the range of lateral displacements. Hence, the results obtained in this work are not restrictive and, in principle, are applicable to 3-D models as well. Although a thorough analysis using 3-D models is possible in FEM and US simulations, we restricted the analysis to only 2-D models because of the challenges involved in making 3-D spheroid inclusion (firmly and loosely bonded to surrounding tissue) phantoms for use in experiments.

In Figure 9 are an example *in vivo* sonogram, axial displacement image, lateral displacement image and RE of an invasive adenocarcinoma (cancer) and a benign fibroadenoma. The REs were subjected to further processing by applying a correlation filter and segmentation threshold before normalization to visualize in −1 to +1 scale. Using the correlation filter, we retain the rotation values only for those pixels having corresponding cross-correlation coefficients >0.75. During segmentation, the rotation values that are higher than a chosen threshold value (*i.e.,* 40% of the maximum rotation value) are retained in the final REs. The maximum rotation value used in the segmentation threshold was calculated as described in Thittai and Xia (2015), and the adaptive strain normalization method developed by Lindop et al. (2008) was adapted for normalization. The displayed axial displacements, lateral displacements and REs were obtained by averaging eight frames. Note that the benign fibroadenoma undergoes rotation and can be contrasted from the background, whereas no such contrast is observed in the case of the adenocarcinoma, which is consistent with what would be expected based on the differences in the lesion–background bonding condition of benign fibroadenoma and malignant lesion in the breast. Moreover, these results are also consistent with the corresponding results from simulations and phantom experiments. These example *in vivo* data were chosen from the database, which was previously reported in Chintada et al. (2017) and, as disclosed therein, were used with institutional review board approval and informed patient consent.

Although most of the cited clinical motivation for visualizing the inclusion bonding condition refers to breast lesions, this information was also found to be useful and applicable to brain lesions (Chakraborty et al. 2012). The use of magnetic resonance elastography (MRE) to assess lesion–brain adhesion non-invasively has been reported (Yin et al. 2015, 2017). The latter authors exploit the fact that in response to an applied shear force, a lesion without adhesion will slip or move freely at a lesion–brain boundary, whereas no relative motion will occur for a lesion that is fixed to the surrounding brain tissue. Thus, the findings regarding the fundamental contrast mechanism reported in this article could be of value even to elastography performed using other modalities.

CONCLUSIONS

The authors examined the amount of rotation undergone by an inclusion embedded in a background, at different settings of mechanical parameters, for both loosely and firmly bonded inclusions. This was studied using FEM and FIELD II simulations and *in vitro* phantom experiments. It is clear from the results that rotation contrast was present only in the case of loosely bonded inclusions and depends on the inclusion asymmetry and inclusion orientation with respect to the axis of deformation.

REFERENCES

Awad SI, Yen JT. 3D strain imaging using a rectilinear 2D array. Ultrason Imaging 2007;29:220–230.

Bamber JC, De Gonzalez L, Cosgrove DO, Simmons P, Davey J, McKinna J. Quantitative evaluation of real-time ultrasound features of the breast. Ultrasound Med Biol 1988;14:81–87.

Barr RG. Breast elastography. New York: Thieme; 2015.

Chakraborty A, Bamber JC, Dorward NL. Slip elastography: A novel method for visualising and characterizing adherence between two surfaces in contact. Ultrasonics 2012;52:364–376.

Chen E, Adler R, Carson P, Jenkins W, O'brien W. Ultrasound tissue displacement imaging with application to breast cancer. Ultrasound Med Biol 1995;21:1153–1162.

Chintada BR, Subramani AV, Raghavan B Thittai AK. A novel elastographic frame quality indicator and its use in automatic representative frame selection from a cine loop. Ultrasound Med Biol 2017;43:258–272.

Correas JM, Tissier AM, Khairoune A, Khoury G, Eiss D, Hélénon O. Ultrasound elastography of the prostate: State of the art. Diagn Interv Imaging 2013;94:551–560.

Deprez JF, Brusseau E, Schmitt C, Cloutier G, Basset O. 3D estimation of soft biological tissue deformation from radio-frequency ultrasound volume acquisitions. Med Image Anal 2009;13:116–127.

Eshelby J. Elastic inclusions and inhomogeneities. In: Sneddon IN, Hill R, (eds). Progress in solid mechanics, vol. 2. Amsterdam: North-Holland; 1961. p. 89–140.

Eshelby JD. The determination of the elastic field of an ellipsoidal inclusion, and related problems. Proc R Soc London A Math Phys Eng Sci 1957;241:376–396.

Fisher TG, Hall TJ, Panda S, Richards MS, Barbone PE, Jiang J, Resnick J, Barnes S. Volumetric elasticity imaging with a 2-D CMUT array. Ultrasound Med Biol 2010;36:978–990.

Fry KE. Benign lesions of the breast. CA Cancer J Clin 1954;4:160–161.

Galaz B, ThitaiKumar A, Ophir J. Axial-shear strain distributions in an elliptical inclusion model: I. A simulation study. In: Proceedings, 8th International Conference on the Ultrasonic Measurement and Imaging of Tissue Elasticity, Vlissingen, The Netherlands, 14–17 September 2009. Austin, TX: ITEC, 2009:99.

Hall TJ, Bilgen M, Insana MF, Krouskop TA. Phantom materials for elastography. IEEE Trans Ultrason Ferroelectr Freq Control 1997; 44:1355–1365.

Hansen H, Lopata R, Idzenga T, de Korte CL. Full 2D displacement vector and strain tensor estimation for superficial tissue using beam-steered ultrasound imaging. Phys Med Biol 2010;55:3201.

Jensen JA. A model for the propagation and scattering of ultrasound in tissue. J Acoust Soc Am 1991;89:182–190.

Jensen JA. Field: A program for simulating ultrasound systems. Med Biol Eng Comput 1996;34:351–352.

Kallel F, Prihoda CD, Ophir J. Contrast-transfer efficiency for continuously varying tissue moduli: Simulation and phantom validation. Ultrasound Med Biol 2001;27:1115–1125.

Konofagou E, Ophir J. A new elastographic method for estimation and imaging of lateral displacements, lateral strains, corrected axial strains and poissons ratios in tissues. Ultrasound Med Biol 1998;24:1183–1199.

Konofagou EE, Harrigan T, Ophir J. Shear strain estimation and lesion mobility assessment in elastography. Ultrasonics 2000;38:400–404.

Kothawala A, Chandramoorthi S, Reddy NRK Thittai AK. Spatial compounding technique to obtain rotation elastogram: A feasibility study. Ultrasound Med Biol 2017;43:1290–1301.

Lindop JE, Treece GM, Gee AH, Prager RW. Estimation of displacement location for enhanced strain imaging. IEEE Trans Ultrason Ferroelectr Freq Control 2007;54:1751–1771.

Lindop JE, Treece GM, Gee AH, Prager RW. An intelligent interface for freehand strain imaging. Ultrasound Med Biol 2008;34:1117–1128.

Lokesh B, Chintada BR, Thittai AK. Rotation elastogram estimation using synthetic transmit-aperture technique: A feasibility study. Ultrason Imaging 2017;39:189–204.

Lopata RG, Nillesen MM, Hansen HH, Gerrits IH, Thijssen JM, De Korte CL. Performance evaluation of methods for two-dimensional displacement and strain estimation using ultrasound radio frequency data. Ultrasound Med Biol 2009a;35:796–812.

Lopata RG, Nillesen MM, Hansen HH, Thijssen JM, De Korte CL. Performance of RF-based 2D strain imaging techniques in deforming structures with large shearing and rotational movement. In: Proceedings, Eighth International Conference on the Ultrasonic Measurement

and Imaging of Tissue Elasticity, Vlissingen, The Netherlands, 2009b: 72.

Lubarda V, Markenscoff X. On the stress field in sliding ellipsoidal inclusions with shear eigenstrain. J Appl Mech 1998;65:858–862.

Mura T, Furuhashi R. The elastic inclusion with a sliding interface. J Appl Mech 1984;51:308–310.

Ophir J, Cespedes I, Ponnekanti H, Yazdi Y, Li X. Elastography: A quantitative method for imaging the elasticity of biological tissues. Ultrason Imaging 1991;13:111–134.

Ophir J, Alam S, Garra B, Kallel F, Konofagou E, Krouskop T, Varghese T. Elastography: Ultrasonic estimation and imaging of the elastic properties of tissues. Proc Inst Mech Eng H 1999;213:203–233.

Shi H, Varghese T. Two-dimensional multi-level strain estimation for discontinuous tissue. Phys Med Biol 2007;52:389.

Shiina T. JSUM ultrasound elastography practice guidelines: Basics and terminology. J Med Ultrason (2001) 2013;40:309–323.

Stavros AT, Thickman D, Rapp CL, Dennis MA, Parker SH, Sisney GA. Solid breast nodules: Use of sonography to distinguish between benign and malignant lesions. Radiology 1995;196:123–134.

Techavipoo U, Chen Q, Varghese T, Zagzebski JA. Estimation of displacement vectors and strain tensors in elastography using angular insonifications. IEEE Trans Med Imaging 2004;23:1479–1489.

Thitaikumar A, Krouskop TA, Garra BS, Ophir J. Visualization of bonding at an inclusion boundary using axial-shear strain elastography: A feasibility study. Phys Med Biol 2007;52:2615.

Thitaikumar A, Mobbs LM, Kraemer-Chant CM, Garra BS, Ophir J. Breast tumor classification using axial shear strain elastography: A feasibility study. Phys Med Biol 2008;53:4809.

Thittai AK, Xia R. An analysis of the segmentation threshold used in axial-shear strain elastography. Ultrasonics 2015;55:58–64.

Thittai AK, Galaz B, Ophir J. Axial-shear strain distributions in an elliptical inclusion model: Experimental validation and in vivo examples with implications to breast tumor classification. Ultrasound Med Biol 2010;36:814–820.

Thittai AK, Yamal JM, Mobbs LM, Kraemer-Chant CM, Chekuri S, Garra BS, Ophir J. Axial-shear strain elastography for breast lesion classification: Further results from in vivo data. Ultrasound Med Biol 2011;37:189–197.

Thittai AK, Galaz B, Ophir J. On the advantages of imaging the axial-shear strain component of the total shear strain in breast tumors. Ultrasound Med Biol 2012;38:2031–2037.

Timoshenko SP, Goodier JN. Theory of elasticity, 3rd ed. New York: McGraw-Hill; 1970.

Treece G, Lindop J, Gee A, Prager R. Near-real-time 3D ultrasonic strain imaging. In: Akiyama I, (ed). Acoustical imaging. Dordrecht: Springer; 2008. p. 27–32.

Ueno E, Tohno E, Soeda S, Asaoka Y, Itoh K, Bamber J, Blaszqzyk M, Davey J, McKinna J. Dynamic tests in real-time breast echography. Ultrasound Med Biol 1988;14:53–57.

Varghese T, Ophir J. A theoretical framework for performance characterization of elastography: The strain filter. IEEE Trans Ultrason Ferroelectr Freq Control 1997;44:164–172.

Yin Z, Glaser KJ, Manduca A, Van Gompel JJ, Link MJ, Hughes JD, Romano A, Ehman RL, Huston JIII. Slip interface imaging predicts tumor brain adhesion in vestibular schwannomas. Radiology 2015;277:507–517.

Yin Z, Hughes JD, Glaser KJ, Manduca A, Van Gompel J, Link MJ, Romano A, Ehman RL, Huston J. Slip interface imaging based on MR-elastography preoperatively predicts meningioma–brain adhesion. J Magn Reson Imaging 2017;46:1007–1016.